

Article

The Study of Turbulent Fluctuation Characteristics in a Small Rotary Engine with a Peripheral Port Based on the Improved Delayed Detached Eddy Simulation Shear-Stress Transport (IDDES-SST) Method

Yan Zhang, Jinxiang Liu * and Zhengxing Zuo

School of Mechanical Engineering, Beijing Institute of Technology, Beijing 100081, China; zy2724@126.com (Y.Z.); zxzuo@bit.edu.cn (Z.Z.)

* Correspondence: liujx@bit.edu.cn; Tel.: +86-010-6891-1392

Received: 8 February 2018; Accepted: 2 March 2018; Published: 14 March 2018

Abstract: In this paper, an improved delayed detached eddy simulation method combined with shear-stress transport (SST) model was used to study the three-dimensional turbulent characteristics in a small rotary engine with a peripheral port. The turbulent characteristics including instantaneous velocity, turbulent fluctuation, coherent structure and velocity circulation were analysed based on a dynamic model of the small rotary engine. Three sets of conclusions on the basis of computational results were obtained. First, it was found that large-scale vortex structures with high intensity were distributed in the center of the chamber in the intake process and broke into lots of small vortex structures in the compression process. Second, flow stability in the X direction decreased from the leading to the trailing in the small rotary engine. The fluctuation velocity of the Y direction showed the paraboloid feature and its peak position moved from the mid-back to the middle of the chamber during the operation process. Third, during the intake process, two vortices occurred in the cross section parallel to the covers and were located at the leading and trailing of the cross section, respectively. Compared to the intake process, more vortices occur at cross sections which were far away from the central section during the compression process.

Keywords: small rotary engine; coherent structure; velocity circulation; turbulent fluctuation

1. Introduction

Rotary engines offer higher power density, lower vibration and fewer part counts than conventional reciprocating engines [1,2]. Based on these advantages, the rotary engine has wide prospective applications for unmanned aerial vehicles, portable devices, and generator units in military and civil fields [3]. The problem of very low thermal efficiency in rotary engine has not yet been solved. A small rotary engine due to a large surface-to-volume ratio aggravates this problem. Previous investigations have suggested that thermal efficiency is closely related to the mechanism of the flow field [4–7]. Due to the long and narrow space of the chamber and high-speed rotation of the rotor, turbulence is the most prominent feature in the flow field. In order to improve the thermal efficiency in a small rotary engine, an examination of the turbulent characteristics of the flow field is particularly necessary.

For numerical simulation, the transient turbulent characteristics of the conventional reciprocating engine have already been investigated through large eddy simulation (LES) [8–11]. Although LES is considered a high-fidelity method, it requires a huge amount of computational expense [12]. In order to obtain accurate results and save computational cost, detached eddy simulation (DES) combining the Reynolds-average Navier Stoke (RANS) and LES has been developed [13]. The DES simulated

the small eddies near the boundary using RANS and the large eddies in the far field using LES [14]. For wall-bounded flows, the flow instability was too weak so that it required many boundary-layer thicknesses to obtain a sufficiently developed turbulence [15]. Based on this background, a DES shear-stress transport (SST) model was proposed [16]. The DES-SST model has been used to predict turbulent characteristics in a simplified engine setup [17]. The velocity field was analyzed for both computation and experiment with a special emphasis on the useability of the DES-SST model to predict turbulent fluctuations, and the turbulent length scale was determined. Then, the DES-SST model was successfully applied to the investigation of turbulent fluctuation in a gasoline engine [18]. The study made a comparison between the instantaneous velocity field and experimental measurements during the intake and compression stroke in a single cycle. Good agreement between the magnitudes of the large-scale fluctuation resolved by both the DES-SST and the PIV experiment was obtained. Furthermore, an improved delayed detached eddy simulation (IDDES) SST model was developed based on the classical DES-SST model [19]. It improved the inaccurate treatment in the grid-induced separation for the DES-SST. In a small rotary engine, high rotating speed aggravates air flow instability and the chamber space changes in a form of irregularity. Both of them increase the complexity of turbulence in a small rotary engine.

For all the reasons mentioned above, the main purpose of this paper is to study turbulent characteristics with the IDDES-SST model combined with the Q-criterion. For the definition of the Q-criterion, refer to Section 2.4. Unstructured deforming mesh and sliding three-dimension mesh are adopted. A user defined function (UDF) invoked by commercial CFD software FLUENT is used to define the movement of the mesh. In order to present the advantages of the IDDES-SST model, the results acquired by RANS are also shown. This paper focuses on the investigation of the instantaneous velocity, turbulent fluctuation, coherent structure and velocity circulation at 15,000 r/min in a small rotary engine.

2. Mathematical Model

2.1. Improved Delayed Detached Eddy Simulation (IDDES) Model

The IDDES method is used as the turbulence model to simulate the turbulence characteristics of a small rotary engine. In this model, the modified Menters SST two-equation eddy viscosity [20] is used as the RANS model. The modification of the RANS model is the dissipation-rate term of the turbulent-kinetic energy (TKE) transport equation. The TKE equation can be written as:

$$\frac{\partial(\rho\kappa)}{\partial t} + \frac{\partial(\rho u_j \kappa)}{\partial x_j} = \frac{\partial}{\partial x_j} \left[\left(\mu + \frac{1}{\sigma} \mu_t \right) \frac{\partial \kappa}{\partial x_j} \right] + \tau_{ij} S_{ij} - \frac{\rho \kappa^{3/2}}{L_{IDDES}} \quad (1)$$

The L_{IDDES} defined as IDDES length scale, can be written as:

$$L_{IDDES} = \tilde{f}_d(1 + f_e)L_{RANS} + (1 - \tilde{f}_d)L_{LES} \quad (2)$$

$$L_{RANS} = \frac{\kappa^{1/2}}{\beta^* \omega'}, L_{LES} = C_{DES} \Delta \quad (3)$$

$$\Delta = \min\{\max\{C_w \Delta_{\max}, C_w d, \Delta_{\min}\}, \Delta_{\max}\} \quad (4)$$

C_{DES} is an important parameter to describe the turbulent scale length. The corresponding value C_{DES} should be calibrated by either branch of both the $\kappa - \varepsilon$ and the $\kappa - \omega$ branches that exist in the SST-based mode [17]. The $\kappa - \varepsilon$ branch is dominant, because the LES mode of the IDDES-SST is mostly away from the wall. The value of C_{DES} is determined as:

$$C_{DES} = (1 - F_1)C_{DES}^{\kappa-\varepsilon} + F_1 C_{DES}^{\kappa-\omega} \quad (5)$$

2.2. Flow-Field Decomposition

The velocity of the flow field can be divided into mean velocity and turbulent fluctuation velocity [21,22], shown as:

$$\vec{U} = \vec{U}_{EA} + \vec{U}_F \quad (6)$$

$$\vec{U}_{EA} = \frac{1}{N} \sum_{i=1}^N \vec{U} \quad (7)$$

2.3. Velocity Circulation

Vorticity is the tendency for elements of the fluid to ‘spin’ [21]. For a small area of fluid flow A , vorticity can be calculated by:

$$dJ = W_{ij} \cos(\vec{\omega}, \vec{n}) dA = W_{ij} dA \quad (8)$$

On the other hand, vorticity is related to circulation in a fluid by the Stokes’ theorem:

$$\Gamma_L = 2J = 2 \int_A W_{ij} dA \quad (9)$$

2.4. Q-Criterion

The Q-criterion is most wide and simplest method to identify coherent structures in an engine [23]. A coherent structure is defined as a turbulent flow containing orderly components that can be described as being instantaneously coherent over the spatial extent of the flow structure. The Q-criterion is used to describe the vortex structures by iso-surface using a specified Q value. The Q is a second invariant with regard to the velocity gradient tensor, defined as [24]:

$$Q = \frac{1}{2} (W_{ij} W_{ij} - S_{ij} S_{ij}) \quad (10)$$

$$S_{ij} = \frac{1}{2} \left(\frac{\partial u_i}{\partial x_j} + \frac{\partial u_j}{\partial x_i} \right) \quad (11)$$

$$W_{ij} = \frac{1}{2} \left(\frac{\partial u_i}{\partial x_j} - \frac{\partial u_j}{\partial x_i} \right) \quad (12)$$

3. Geometric Model and Dynamic Meshing

3.1. Geometric Model

In the present study, a geometric model that has the small rotary naturally aspirated is established. The rotor revolves both round the center of the cylinder and on its own axis. The rotation speed ratio between the rotor and the eccentric shaft is 1:3. The schematic diagram of the small rotary engine is shown in Figure 1. The coordinates of X, Y and Z are established in the central plane. The technical parameters of the engine are listed in Table 1.

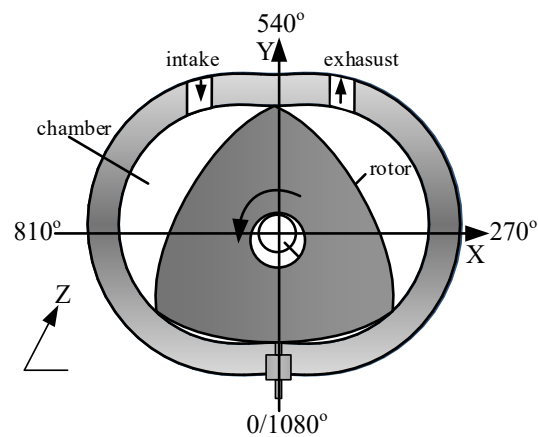


Figure 1. Schematic of small rotary engine.

Table 1. Small rotary engine specifications.

Parameter	Value
Generating radius	21 mm
Eccentricity	3 mm
Displacement	5 mL
Compression ratio	8.5
Width	14.5 mm
Intake phase	Advanced angle, 459° BTDC; Delay angle, 220° ATDC
Exhaust phase	Advanced angle, 198° BTDC; Delay angle, 486° ATDC

3.2. Dynamic Meshing

Since the work processes of the three chambers are the same and computation needs to save cost, only one chamber is selected for the simulation. Considering the operating characteristics of the small rotary engine, the peripheral intake and exhaust ports are static due to having no moving parts. The combustion chamber is modeled with the dynamic mesh according to the movement characteristics of the engine. For the dynamic mesh, unstructured mesh is adopted. The mesh element is set to 0.2 mm and the grid compression arithmetic near the wall is used. The total mesh number is up to 1,050,000 at 360° BTDC, shown in Figure 2.

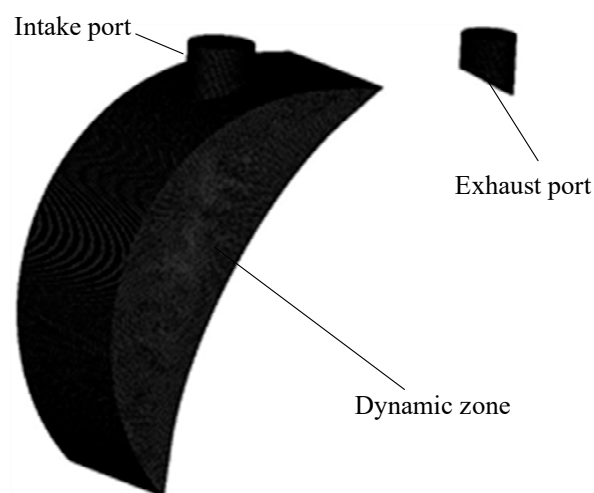


Figure 2. Computation mesh.

For the dynamic mesh, DEFINE_CG_MOTION and DEFINE_GRID_MOTION are used to specify the motion of the dynamic zone in FLUENT 16.0 by providing the velocities and grid update at each time step.

4. Boundary Conditions and IDDES Model Validation

4.1. Determination of Time Step Size

IDDES-SST simulations yield ensemble-averaged flow fields. This allows the use of a large time step if implicit temporal schemes are used, which leads to an essential decrease of computer processing unit (CPU) time. The physical time scales for a certain flow configuration are not always known in advance. Therefore, an appropriate time step size is very important for implicit temporal schemes. The time step size is determined based on the highest velocity U_{\max} , the smallest grid spacing Δ_{\min} , and an acoustic Courant–Friedrich–Lewy (CFL) number. The highest velocity can be estimated with 1.5–5 times the average velocity U_{avg} acquired by a prior RANS simulation. These considerations are taken into the following the expression for the time step size [17]:

$$\Delta t = CFL \cdot \frac{\Delta x_{\min}}{U_{\max}} = CFL \cdot \frac{\Delta x_{\min}}{1.5 \cdot U_{\text{avg}}} \quad (13)$$

4.2. Computing Model and Boundary Condition

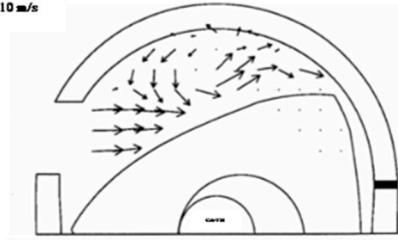
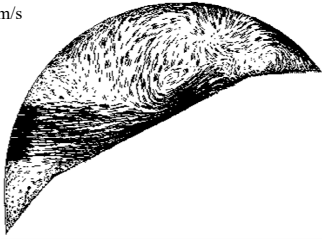
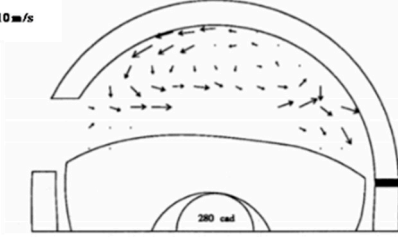
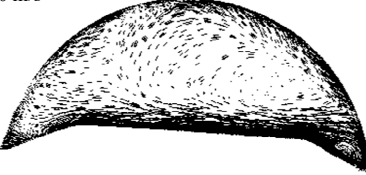
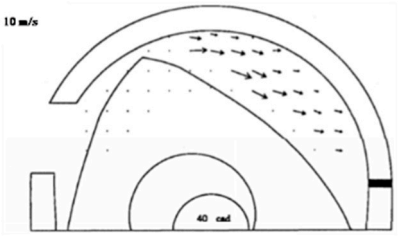
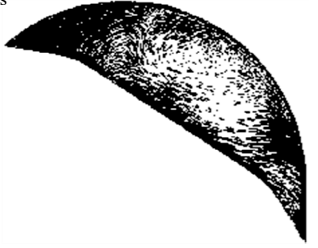
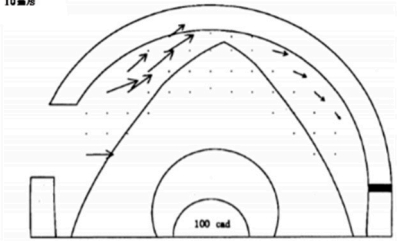
The simulations are based on the IDDES-SST model. The ideal gas law, constant thermal conductivity and viscosity are assumed. Pressures at the inlet and outlet are defined. The engine is naturally aspirated, hence the values of the pressure are set to atmospheric pressure. The first-order upwind scheme is used to discretize the turbulent kinetic energy and turbulent dissipation. The second order upwind scheme is used to discretize the energy and density. The bounded central differencing is used to discretize the momentum. The time step size is set to 2.5×10^{-6} s and max iterations are set to 1000 at 15,000 r/min. The determination of $C_{DES}^{\kappa-\epsilon}$ and $C_{DES}^{\kappa-\omega}$ have been explained and successfully applied to the flow investigation in an engine [17]. Therefore, $C_{DES}^{\kappa-\epsilon} = 0.61$ and $C_{DES}^{\kappa-\omega} = 0.78$ are suitable values for the present study.

4.3. Experimental Results

The calculated flow mathematical model is validated by experimental results described in DeFilippis et al. [25]. The selected locations are in the rotor-housing central plane. The same symmetrical recesses are used for the simulation and the experimental test.

Table 2 shows the comparison of the simulation results with the experimental data. For four different crankangles (CA), the simulation results are in good agreement with the experimental data. For example, when the CA is at 730° , the fluid forms the swirl at the front of the combustion chamber. Both of them have the same flow phenomenon. When the CA is at 1000° , the unidirectional flow is observed because of the reduction for chamber volume. The simulation results with the experimental data are in good agreement at other CAs.

Table 2. Comparison of the experimental data with the simulation results.

CA/°	Experimental Results	Simulation Results
730		
820		
910		
1000		

5. Results and Discussion

5.1. Velocity Field

The averaged and instantaneous 3D velocity field within the cylinder are computed by the RANS and IDDES-SST model, respectively. Figure 3 shows the location of cross sections for comparison. The cross sections are obtained by slices located in Y-planes. The location of the cross sections is $Y = -6$ mm and $Y = -10$ mm, respectively. Figure 4 compares the computed time-averaged X-velocity component for RANS and the instantaneous velocity component for IDDES-SST in different cross sections. By comparing the velocity field between Figure 4b,d, an impression of the resolved velocity fluctuations can be obtained for the instantaneous velocity values. The flow fields form the closed zones that interact with each other. It is important to note that no such fluctuations can be found in the RANS calculation. At $Y = -6$ mm, the flow velocity near the pocket is relatively large, as shown in Figure 4a,c. Comparing Figure 4a,b, it can be seen that the velocity at the central zone increases from

$Y = -6$ mm to $Y = -10$ mm. The results indicate that strong turbulence may be occurred at the leading of the chamber.

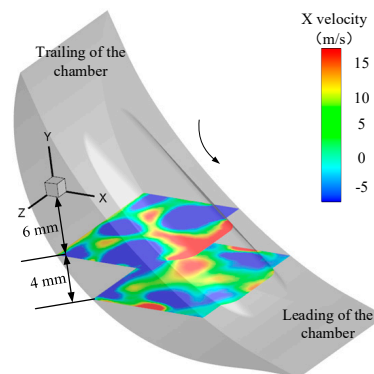


Figure 3. Location for comparison at 135° BTDC.

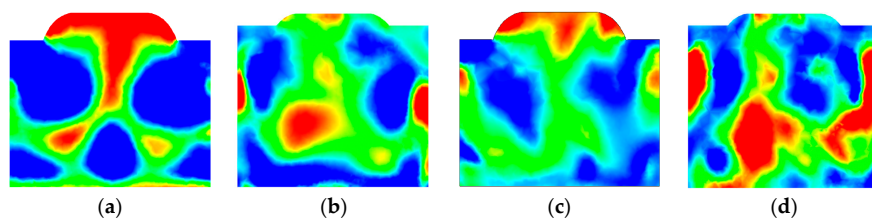


Figure 4. Velocity field in X velocity at 145° BTDC. (a,b) Averaged velocity field for RANS at $Y = -6$ mm and $Y = -10$ mm, respectively; (c,d) instantaneous velocity field for improved delayed detached eddy simulation shear-stress transport (IDDES-SST) at $Y = -6$ mm and $Y = -10$ mm, respectively.

In order to study the instantaneous field near the intake port, the location of the cross section is shown in Figure 5 and remains fixed. Figure 6 shows instantaneous X velocity development in the cross section through the intake port during the intake stroke. During the initial phase of the intake stroke shown by Figure 6a, two reverse vortices with the same radius can be observed at one side of the cross section. The space between the intake port and the rotor is small and the gas velocity from the intake port is very large; therefore, the gas has to divide into two strands due to not having enough development space after the high-speed gas hits the surface of the rotor. The radius of anticlockwise vortices A increase and the clockwise vortices move toward the top of the cross section in Figure 6b. In this stage, since the radius of A becomes large, the space at both sides is squeezed. The top near the intake port has space for the formation of the small vortex structures. Several small vortex structures without a dominant flow direction can be observed at both sides of cross section in Figure 6c. The formation of these vortices is the result of the partial gas flow of A hitting the wall. At the end of the intake process, small vortex structures diminish and only two large-scale vortices can be observed in Figure 6d.

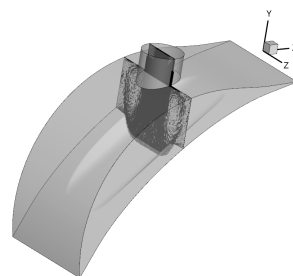


Figure 5. Location of cross section.

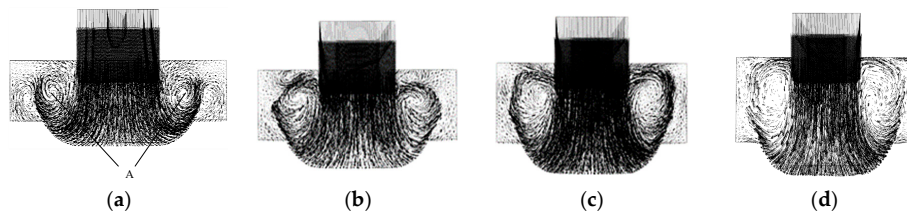


Figure 6. Instantaneous velocity field of cross section at different CA. (a) CA = 470° BTDC; (b) CA = 450° BTDC; (c) CA = 430° BTDC; (d) CA = 410° BTDC.

5.2. Coherent Structure

The identification of coherent structure can be realized by the Q-criterion. The value of Q represents the intensity of the vortex. High transient and intensity flow characteristics occur due to the high-speed operation of the small rotary engine, so choosing a reasonable value for Q is necessary. The Q-criterion is used to reflect vortex structures by defining the iso-surface using a specified Q value; so the Q selected within appropriate value ranges can be accepted. Figure 7 shows the vortex field at 360° BTDC under different Q values. At $Q = 10^6 \text{ s}^{-1}$ shown in Figure 7a, the vortices of the chamber are in chaos so that the vortices with high intensity cannot be filtered out. As $Q = 10^8 \text{ s}^{-1}$ shown in Figure 7c, the vortex field is unable to fully reflect the characteristics of a coherent structure. By comparing and screening, the $Q = 10^7 \text{ s}^{-1}$ is the appropriate value. In Figure 7b, it can be seen that there are large numbers of vortices with different features in the whole combustion chamber. In this condition, the characteristics of coherent structure are fully demonstrated.

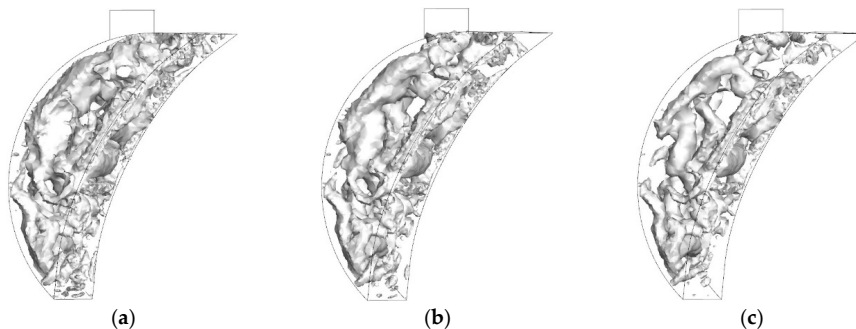


Figure 7. Vortex fields at 360° BTDC under different Q values. (a) $Q = 10^6 \text{ s}^{-1}$; (b) $Q = 10^7 \text{ s}^{-1}$; (c) $Q = 10^8 \text{ s}^{-1}$.

The coherent structure in the chamber will change with the operation of the engine. Vortex fields with different CA at 15,000 r/min are shown in Figure 8. In the intake process shown in Figure 8a, large numbers of vortices distribute in the whole space of the chamber and the scale length of vortices at the central zone is relatively large. The intake charge and velocity is large so that a large amount of gas flow gathers in the center of the chamber. The number of vortices in the trailing is small due to the rotation direction of the rotor. At the end of the intake stroke shown in Figure 8b, it can be found that reverse vortices with high intensity form in the intake port and the number of vortices in the leading increases compared to that at CA = 360° BTDC. In the compression stroke at 135° BTDC, as shown Figure 8c, the scale length of vortices decreases further. Large scale vortices formed in the intake process begin to deform and break up, leading to a more small-scale length of vortices formed in the chamber. At 135° BTDC, turbulence has been fully developed. Therefore, the ignition time set at 135° BTDC may be a good choice for the small rotary engine. At 450° BTDC, most of the vortices break up further and eventually disappear. This is because that very small space is unable to maintain the development of the vortices. It can also found that in the leading of the chamber vortices hardly exist.

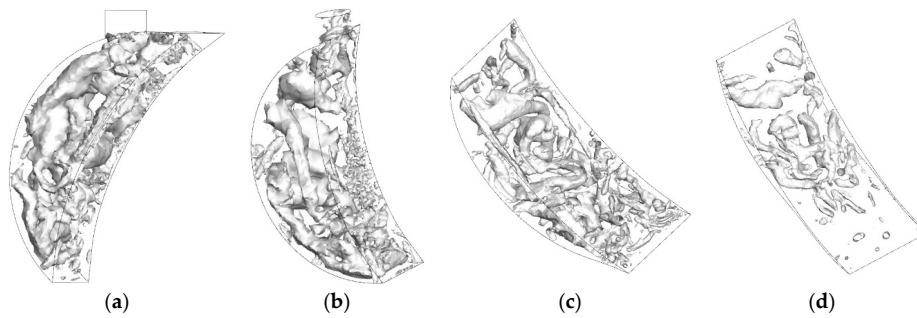


Figure 8. Vortex fields with different CA at 15,000 r/min ($Q = 10^7 \text{ s}^{-1}$). (a) CA = 360° BTDC; (b) CA = 245° BTDC; (c) CA = 135° BTDC; (d) CA = 45° BTDC.

5.3. Velocity Fluctuation

Velocity fluctuation is one of the most important flow characteristics in a small rotary engine. The relative magnitude of fluctuation velocity suggests flow stability, so the root-mean-square (RMSE) is selected to represent the velocity fluctuation. The RMS of fluctuating velocity in the central plane parallel to the cover is shown in Figure 9. The plane geometric scheme corresponding to the crankshaft angle can also be seen in Figure 9. It can be found that the fluctuation velocity RMS of the X direction decreases from the leading to the trailing as shown in Figure 9a,c. Its maximum is 33 m/s and minimum is 9 m/s at 450° BTDC. The maximum reduces to 30 m/s and 8 m/s at 205° BTDC. The results indicate that the kinetic energy of the X direction has no significant dissipation. The velocity fluctuation peak of the Y direction occurs at the mid-back as CA is at 450° BTDC in Figure 9b. The value is up to 21 m/s. The velocity fluctuation peak of the Y direction occurs at the middle as CA is at 205° BTDC in Figure 9d. The value is up to 28 m/s and the distribution of Y velocity RMS is like a paraboloid.

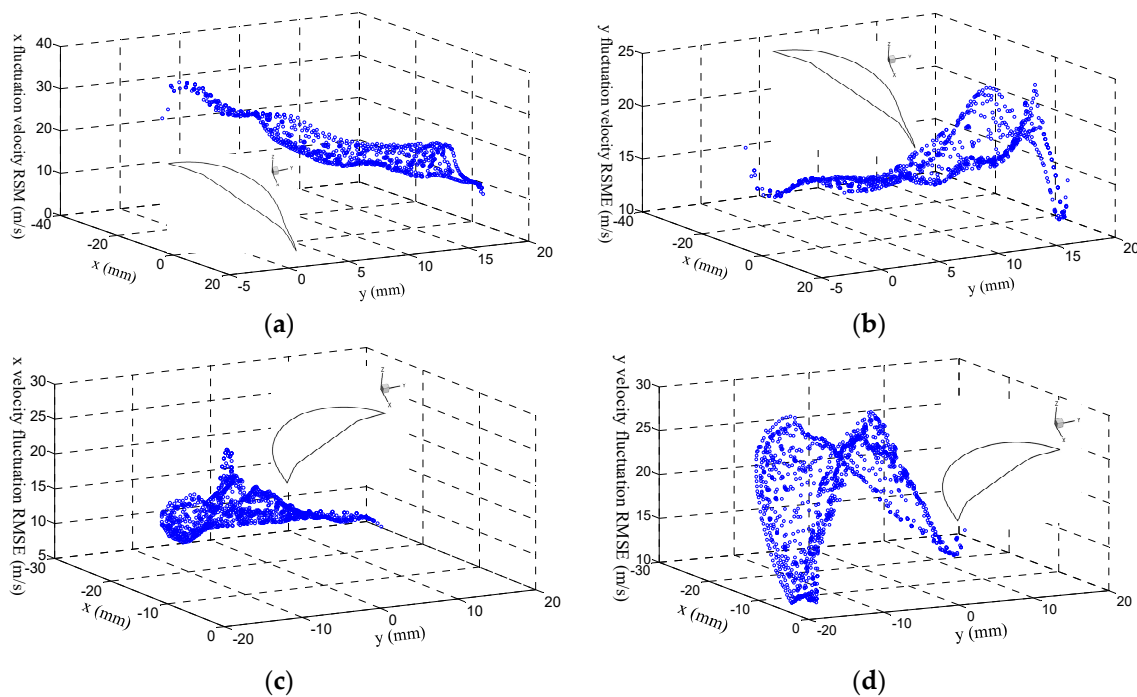


Figure 9. Root-mean-square (RMS) of velocity fluctuation. (a) RMS of X velocity fluctuation at 450° BTDC; (b) RMS of Y velocity fluctuation at 450° BTDC; (c) RMS of X velocity fluctuation at 205° BTDC; (d) RMS of Y velocity fluctuation at 205° BTDC.

5.4. Velocity Circulation

The center and radius of the swirl are determined based on point-based methods [21,23], which are computationally less expensive and more accurate but time-consuming. Swirls in the rotary engine are continuously changing in a whole cycle. Therefore, the swirl radius, swirl center and swirl ratio are continuously changing with the rotation of the rotor. Figure 10 shows the velocity vector field on the different Z planes and streamlines in the vortex circle under different CA. The Z axis is perpendicular to the cover of the engine shown in Figure 1. $Z = 0$ represents the middle plane in the chamber. There are two obvious vortices in the Z plane shown in Figure 10a. One is at the leading of the chamber, the other is at the trailing of the chamber. The circular zones show the streamlines and the contour of velocity. At 450° BTDC, the radius and velocity magnitude of 1 are 0.6 mm larger than that of 2. With the variation of the distance from the center plane to the cover, the central position and radius of the vortex have moved, as shown by Figure 10b. The radius of 2 at $Z = 0$ is 0.45 mm larger than that at $Z = 4$. The intake port is in the middle of the chamber at the Z direction. The fresh charge and gas-flow velocity are relatively large and the rotor moves counter-clockwise. Therefore, more air flow comes together in the leading of the chamber so that the radius of 1 at $Z = 0$ mm is 0.6 mm larger than that at $Z = 4$. The air flow from the trailing is obstructed by high-speed airflow from intake port, so the airflow moves toward the two sides of the chamber and then toward the front of the chamber. It is found that vortex 1 disappears at $Z = 6$ by numerical simulation. At 202° BTDC, the gas is compressed in Figure 10c,d. The vortex centers close to the cylinder wall at $Z = 0$ mm and close to the rotor wall at $Z = 4$ mm. There are three vortex centers in the plane at $Z = 4$ mm. Large high-speed airflow in the middle of the chamber hits the walls to form a greater number of vortices. Previous swirls formed by the trailing airflow due to the obstruction of the intake airflow have been broken up. Therefore, three vortex centers are present in the plane at $Z = 4$ mm. At the plane in $Z = 4$ mm, the rotation directions of 1 and 2 are counterclockwise and the rotation directions of 1 and 2 are clockwise.

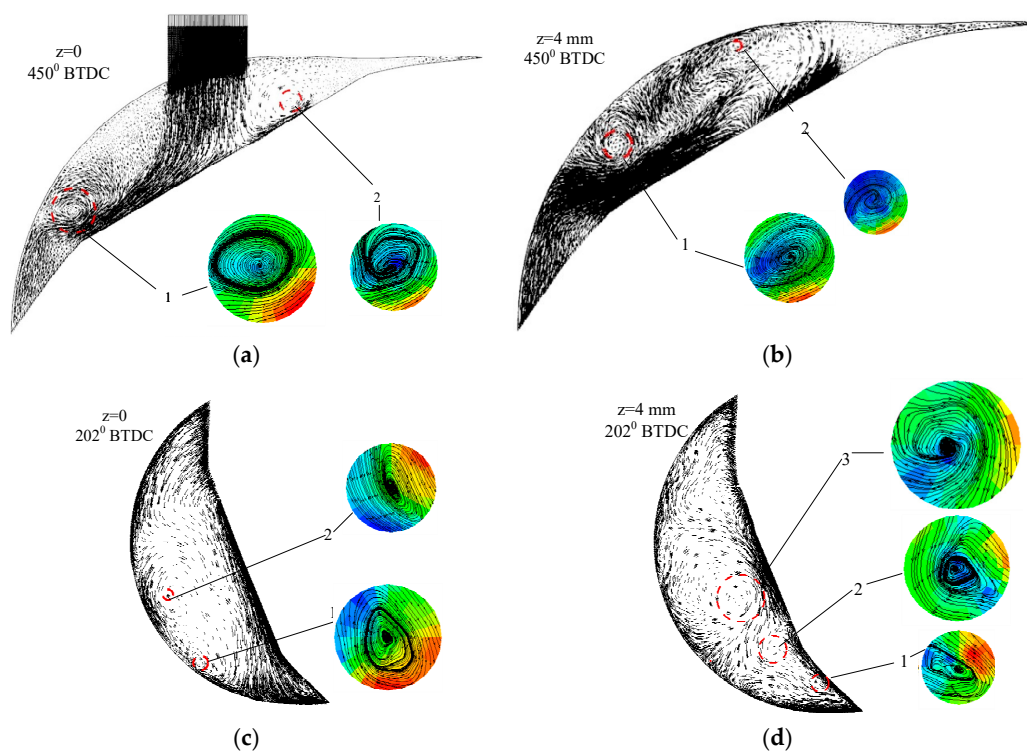


Figure 10. Velocity vector field on the z plane and streamlines in the vortex circle under different CA. (a) $Z = 0$ mm, CA = 450° BTDC; (b) $Z = 4$ mm, CA = 450° BTDC; (c) $Z = 0$ mm, CA = 205° BTDC; (d) $Z = 0$ mm, CA = 205° BTDC.

At 450° BTDC, the position and radius of vortices are shown in Figure 11. The position of vortex center 1 at the X coordinate and Y coordinate increases with the increase of the distance away from the plane at $Z = 0$ mm in Figure 11a,b. This keeps constant substantially as the X direction moves 4 mm along the Y direction. The position of the vortex center 2 produces jumping at plane $Z = 4$ mm. It indicates that the swirls of the region from the $Z = 4$ mm to the cover are generated by the trailing airflow and forms near the walls. The radius of 1 decreases gradually shown by Figure 11c, which suggests swirls breaks up from the middle to the cover. The radius of 1 increases first, then decreases. This is because that high speed airflow from the intake port is helpful for the formation of vortices and accumulates to make the radius become large. The influence of the high speed airflow begins to weaken near the cover, so the radius decreases. Velocity circulation is an important parameter for characterizing the intensity of the vortex field. The counter-clockwise notation is assumed to be positive while defining velocity circulation. Velocity circulation presents a similar curve law with the radius. The value of velocity circulation 1 is close to 0 at the plane $Z = 5$ mm shown by Figure 11d, which suggests that the vortices vanish. The value of velocity circulation 1 is greater than that of 2. The reason for this is that the rotation of the rotor leads to greater airflow coming together in the leading.

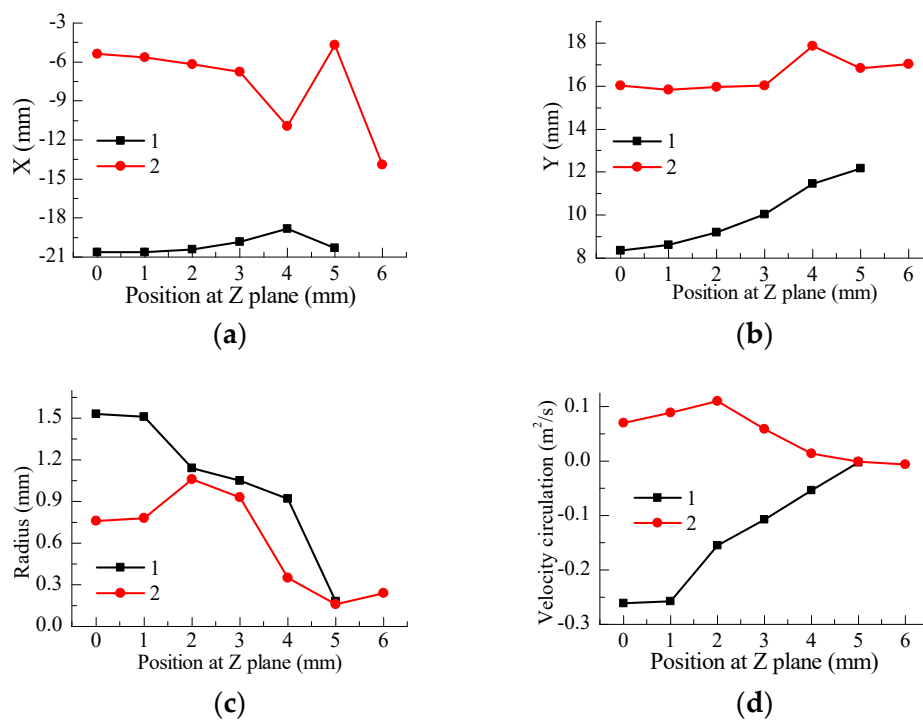


Figure 11. Position and radius of vortex at 450° BTDC. (a) The position of vortex center at X coordinate; (b) the position of vortex center at Y coordinate; (c) vortex radius; (d) velocity circulation.

At 202° BTDC, the number of vortex increases rises to 6 from $Z = 0$ mm to $Z = 6$ mm, as shown in Figure 12. The number first keeps constant, then increases. This shows that the vortices change fairly dramatically. The vortices focus on the leading and middle of the chamber. Large swirls in the middle of the chamber break up to be small swirls, and the number increases. The radius of the vortices is small from $Z = 0$ mm to $Z = 2$ mm and large-radius vortices appear from $Z = 3$ mm to $Z = 7$ mm, as shown in Figure 12a. The maximum radius, 3.5 mm, appears at the plane $Z = 3$ mm. Velocity circulation is negative from $Z = 0$ mm to $Z = 3$ mm and positive from $Z = 4$ mm to $Z = 7$ mm, as shown by Figure 12b. This indicates that vortices in the chamber are formed by different sources and ways. The radius near the middle is small, but the velocity circulation is large. This is due to a large velocity gradient in the middle.

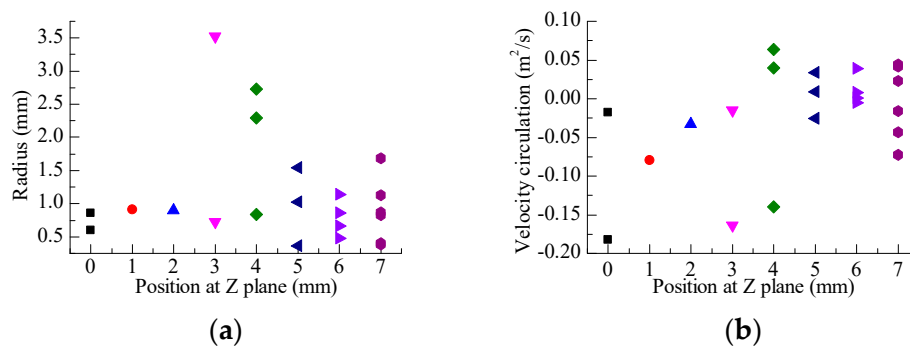


Figure 12. Position and radius of vortex at 202° BTDC. (a) Vortex radius; (b) velocity circulation.

6. Conclusions

In this study, an improved delayed detached eddy simulation method combined with a shear-stress transport model is used to study the three-dimensional turbulent characteristics in a small rotary engine with a peripheral port. Instantaneous velocity, turbulent fluctuation, coherent structure and velocity circulation have been obtained and the main conclusions can be drawn as follows:

- (1) In the initial phase of the intake stroke, two reverse vortices with the same radius form at one side of the intake port. With the operation of the engine, the radius of the clockwise vortices keeps increasing and several small vortex structures without dominant flow direction occur at different positions.
- (2) At 15,000 r/min, the large-scale vortex structures with high intensity mainly gather in the center of the chamber and go through deformation and are broken during the intake process. At 135° BTDC, lots of small vortex structures distribute throughout the whole space of the chamber. Most of the vortices disappear at the end of the compression stroke.
- (3) Flow stability of the X direction increases from the leading to the trailing. The calculated results show the maximum fluctuation velocity RMS at the X direction is mostly four times larger than its minimum at 450° BTDC. The distribution of Y velocity RMS is like a paraboloid and the peak position moves from the mid-back to the middle of the chamber.
- (4) In the intake phase, two vortices occur at the cross section parallel to the covers and are located at the leading and trailing of the cross section, respectively. Compared to the intake process, more vortices occur at cross sections which are far away from the central section during the compression process.

This work is presently concerned with applying an IDDES-SST turbulent model to the small rotary engine, with the aim of predicting turbulent fluctuation during the motored condition. Efforts are also being made to analyse more deeply the simulation outcomes, in particular by predicting velocity fluctuations and coherent structures. The aim is to realize IDDES-SST simulations of a real configuration. Turbulent fluctuation is an important issue in rotary-engine development. According to the results, the distribution of turbulent fluctuation in the whole chamber is significantly non-uniform. Turbulent fluctuation variations are important, since these variations can decide whether the condition (gas motion and composition) in the combustion chamber and, especially, in the vicinity of the spark plug are favorable for stable ignition and flame propagation or not. Moreover, the mixture can fail to ignite or the flame is quenched directly after ignition, which is undesirable in terms of engine roughness, efficiency and unburned hydrocarbon emissions. This condition is significantly influenced by the turbulent fluctuation generated during the intake process, which is determined by the shape of the intake port and the design of both the intake port and the combustion chamber.

Author Contributions: Yan Zhang wrote the main body of the paper; Jinxiang Liu, Zhengxing Zuo revised the paper; Yan Zhang and Jinxiang Liu analyzed the data. All authors read and approved the manuscript. The authors would like to thank the reviewers for their valuable comments on this research.

Conflicts of Interest: The authors declare no conflict of interest.

Nomenclature

N	cycle number
\vec{U}_{EA}	mean velocity
\vec{U}	transient fluctuation velocity
\vec{U}_F	fluctuation velocity
Γ_L	velocity circulation
u_i, u_j	fluctuation velocity magnitude at X, Y
x_i, x_j	X, Y coordinate X, Y coordinate
W_{ij}	vorticity
J	vortex intensity
S_{ij}	mean strain rate tensor
τ_{ij}	tensor of stress
κ	turbulent kinetic energy
t	time
L	a certain close curve
L_{IDDES}	IDDES length scale
L_{RANS}	RANS length scale
L_{LES}	LES length scale
Δ	grid scale
C_w	empirical constant
C_{des}	factor of length scale
d	distance to the nearest wall
\tilde{f}_d	empirical delay function
f_e	elevating function
F_1	first blending function of the SST

Greek Letters

ρ	density
μ	molecular viscosity
μ_t	turbulent viscosity
σ	blending function
β^*	constant value

Acronyms

LES	large eddy simulation
RNS	Reynolds-average Navier Stoke
LDV	laser doppler velocimetry
BTDC	before top dead center
ATDC	after top dead center
RNG	renormalization group
CA	crank angle
DES	mean strain rate tensor
IDDES	improved delayed detached eddy simulation
TKE	turbulent kinetic energy
SST	shear-stress transport
PIV	particle image velocimetry

References

1. Picard, M.; Tian, T.; Nishino, T. Predicting gas in the rotary engine—Part I: Apex and corner seals. *ASME* **2016**, *138*, 1–8. [[CrossRef](#)]
2. Picard, M.; Tian, T.; Nishino, T. Predicting gas in the rotary engine—Part II: Side seals and summary. *ASME* **2016**, *138*, 1–8. [[CrossRef](#)]
3. McReynolds. Small engine, an energy perspective. *SAE Pap.* **1979**, 790477. [[CrossRef](#)]
4. Fan, B.W.; Pan, J.F.; Yang, W.M.; An, H.; Tang, A.; Shao, X.; Xue, H. Effects of different parameters on the flow field of peripheral ported rotary engine. *Eng. Appl. Comput. Fluid* **2015**, *9*, 445–457. [[CrossRef](#)]
5. Shih, T.I.P.; Schock, H.J.; Nguyen, H.I.; Stegeman, I.D. Numerical simulation of the flow field in a motored two-dimensional Wankel engine. *J. Propul. Power* **1987**, *3*, 269–276. [[CrossRef](#)]
6. Fan, B.W.; Pan, J.F.; Pan, Z.H.; Tang, A.K.; Zhu, Y.J.; Xue, H. Effects of pocket shape and ignition slot locations on the combustion processes of a rotary engine fueled with natural gas. *Appl. Therm. Eng.* **2015**, *89*, 11–27. [[CrossRef](#)]
7. Fan, B.W.; Pan, J.F.; Tang, A.K.; Pan, Z.H.; Zhu, Y.J.; Xue, H. Experimental and numerical investigation of the fluid flow in a side-ported rotary engine. *Energy Convers. Manag.* **2015**, *95*, 385–397. [[CrossRef](#)]
8. Meloni, R.; Naso, V. An Insight into the Effect of Advanced Injection Strategies on Pollutant Emissions of a Heavy-Duty Diesel Engine. *Energies* **2013**, *6*, 4331–4351. [[CrossRef](#)]
9. Celik, I.; Yavuz, I.; Smirnov, A. Large eddy simulations of in-cylinder turbulence for internal combustion engines: A review. *Int. J. Engine Res.* **2001**, *2*, 119–148. [[CrossRef](#)]
10. Haworth, D.C.; Jansen, K. Large-eddy simulation on unstructured deforming meshes: Towards reciprocating IC engines. *Comput. Fluids* **2000**, *29*, 493–524. [[CrossRef](#)]
11. Wang, T.; Zhang, X.; Xu, J.; Zheng, S.Z.; Hou, S.X. Large-eddy simulation of flame-turbulence interaction in a spark ignition engine fueled with methane/hydrogen/carbon dioxide. *Energy Convers. Manag.* **2015**, *104*, 147–159. [[CrossRef](#)]
12. Lei, H.; Zhou, D.; Bao, Y.; Li, Y.; Han, Z.L. Three-dimensional Improved Delayed Detached Eddy Simulation of a two-bladed vertical axis wind turbine. *Energy Convers. Manag.* **2017**, *133*, 235–248. [[CrossRef](#)]
13. Spalart, P.R.; Jou, W.H.; Strelets, M.; Allmaras, S. Comments on the Feasibility of LES for Wings, and on a Hybrid RANS/LES Approach. In Proceedings of the Advances in DNS/LES, Louisiana Tech University, Ruston, LA, USA, 4–8 August 1997.
14. Sagaut, P. *Large Eddy Simulation for Incompressible Flow: An Introduction*, 3rd ed.; Springer: Paris, France, 2006; pp. 83–89, ISBN 3-540-26344-6.
15. Gritskevich, M.; Garbaruk, A.; Schütz, J.; Menter, F. Development of DDES and IDDES Formulations for the $k-\omega$ Shear Stress Transport Model. *Flow Turbul. Combust.* **2012**. [[CrossRef](#)]
16. Menter, F.R.; Kuntz, M.; Langtry, R. Ten years of industrial experience with the SST turbulence model. In Proceedings of the 4th International Symposium on Turbulence Heat and Mass Transfer, Antalya, Turkey, 12–17 October 2003.
17. Hasse, C.; Sohm, V.; Durst, B. Detached eddy simulation of cyclic large scale fluctuations in a simplified engine setup. *Int. J. Heat Fluid Flow* **2009**, *30*, 32–43. [[CrossRef](#)]
18. Hasse, C.; Sohm, V.; Durst, B. Numerical investigation of cyclic variations in gasoline engines using a hybrid URANS/LES modeling approach. *Comput. Fluids* **2010**, *39*, 25–48. [[CrossRef](#)]
19. Shur, M.L.; Spalart, P.R.; Strelets, M.K.; Travin, A.K. A hybrid RANS-LES approach with delayed-DES and wall-modelled LES capabilities. *Int. J. Heat Fluid Flow* **2008**, *29*, 1638–1649. [[CrossRef](#)]
20. Menter, F.R. Two-equation eddy-viscosity turbulence models for engineering applications. In Proceedings of the AIAA 23rd Fluid Dynamics, Plasma Dynamics, and Lasers Conference, Orlando, FL, USA, 6–9 July 1993; pp. 1598–1605.
21. Liu, D.M.; Wang, T.Y.; Jia, M.; Wang, G.D. Cycle-to-cycle variation analysis of in-cylinder flow in a gasoline engine with variable valve lift. *Exp. Fluids* **2012**, *53*, 585–602. [[CrossRef](#)]
22. Li, Y.; Zhao, H. Characterization of an in-cylinder flow structure in a high-tumble SI engine. *Int. J. Engine Res.* **2004**, *5*, 375–400. [[CrossRef](#)]
23. Heinrich, V. Detection of vortices and quantitative evaluation of their main parameters from experimental velocity data. *Meas. Sci. Technol.* **2001**. [[CrossRef](#)]

24. Hunt, J.C.R.; Wray, A.; Moin, P. Eddies, stream and convergence zones in turbulent flows. In Proceedings of the Center for Turbulence Research Proceedings of the Summer Program, NASA, Stanford University, Stanford, CA, USA, 1 December 1988.
25. DeFilippis, M.; Hamady, F.; Novak, M.; Schock, H. Effects of pocket configuration on the flow field in a rotary engine assembly. *SAE Pap.* **1992**, 920300. [[CrossRef](#)]



© 2018 by the authors. Licensee MDPI, Basel, Switzerland. This article is an open access article distributed under the terms and conditions of the Creative Commons Attribution (CC BY) license (<http://creativecommons.org/licenses/by/4.0/>).